Chinese Chemical Letters 32 (2021) 3180–3184

Contents lists available at ScienceDirect

Chinese Chemical Letters

journal homepage: www.elsevier.com/locate/cclet

Communication

Fabrication of N-CQDs@$W_{18}O_{49}$ heterojunction with enhanced charge separation and photocatalytic performance under full-spectrum light irradiation

Ju Huang, Jiawen Wang, Zhengjia Hao, Chensha Li, Binsong Wang*, Yang Qu

Department of Environmental Science, School of Chemistry and Materials Science, Key Laboratory of Functional Inorganic Material Chemistry, Ministry of Education of the People's Republic of China, Heilongjiang University, Harbin 150080, China

ARTICLE INFO

Article history:
Received 9 December 2020
Received in revised form 17 January 2021
Accepted 5 March 2021
Available online 9 March 2021

Keywords:
Photocatalysis
Full-spectrum light
Tungsten oxide
Localized surface plasmon resonance
Nitrogen-doped carbon quantum dots

ABSTRACT

Increasing the charge separation and the utilization efficiency of sunlight are essential factors in a photocatalytic process. In this study, we prepared crystalline N-CQDs@$W_{18}O_{49}$ heterostructures, through the *in situ* growth of $W_{18}O_{49}$ nanocrystals on nitrogen-doped carbon quantum dots (N-CQDs). N-CQDs@$W_{18}O_{49}$ nanocomposites showed high activity in the photodegradation of ciprofloxacin (CIP) and methyl orange (MO). The photodegradation activity of the optimized N-CQDs@$W_{18}O_{49}$-5 sample was four times higher than that of $W_{18}O_{49}$ under ultraviolet-visible (UV–vis) light irradiation. The photodegradation activity of N-CQDs@$W_{18}O_{49}$-5 sample was two times higher than that of $W_{18}O_{49}$ under near-infrared (NIR) light irradiation. The enhanced photosensitivity of the nanocomposites was attributed to the promotion of charge separation by N-CQDs and the local surface plasmon resonance (LSPR) effect of $W_{18}O_{49}$ under NIR light irradiation. This work provides a promising approach for designing and manufacturing photocatalysts with full-spectral responsiveness and improved charge separation.

Utilizing solar energy to solve environmental and energy-related problems is of increasing attention [1,2]. Photocatalysis has been recognized as a potential solar energy utilization technology that converts it into chemical energy, thus solving problems related to environmental pollution and energy shortage [3]. Most semiconductor photocatalysts, which have been developed in recent years such as TiO_2, ZnS, CdS, and g-C_3N_4, can only be excited efficiently by ultraviolet (UV) and visible (vis) light [4–6]. However, solar light consists of ~3% UV light and ~44% visible light, while infrared light, accounting for ~53% of its spectrum, cannot be utilized efficiently by most photocatalysts [7–9]. Therefore, it is of utmost importance to design photocatalysts that can utilize the full solar spectrum.

Recently, tungsten oxide has been regarded as one of the most promising semiconductor materials in the field of photocatalysis due to its suitable band gap and environmental friendliness [10,11]. $W_{18}O_{49}$, a member of the tungsten oxide family, has a unique localized surface plasmon (LSPR) effect due to the presence of oxygen vacancies (OV), and has considerable absorption in the near-infrared (NIR) region [12–14]. The LSPR effect is based on the collective oscillation of oxygen vacancies on the surface of $W_{18}O_{49}$ that occur after irradiation with visible or NIR light, which can result in the enhancement of photocatalytic activity [15–17]. However, the photocatalytic activity of $W_{18}O_{49}$ is limited by the rapid recombination of photoinduced charge carriers. One possibility to overcome this issue is to construct a heterostructure with another suitable material to obtain high photocatalytic performance.

Carbon materials have the potential of improving the photocatalytic activity by (i) narrowing the bandgap; (ii) decreasing the recombination rate of photogenerated charge carriers; (iii) providing more active sites and higher surface area; (iv) acting as a photosensitizer; (v) prolonging the lifespan of charge carriers." (with appropriate citations to back this up) [18–20]. Carbon quantum dots (CQDs) are suitable for such purposes that have unique optical and electrical characteristics and a diameter of less than 10 nm. Due to the tunable electronic properties caused by the quantum confinement effect, CQDs can act as active sites and adjust the properties of electrochemical interfaces [21,22]. The recent research work showed that the presence of N in nitrogen-doped CQDs (N-CQDs) could more effectively induce the charge delocalization, reduce work function, and improve photocatalytic

* Corresponding author.
E-mail address: wangbinsong@hlju.edu.cn (B. Wang).

https://doi.org/10.1016/j.cclet.2021.03.018

performance [23,24]. Meanwhile, the work of Ji *et al.* demonstrated that the addition of N-CQDs could adjust the concentration of reactive oxygen species [25]. Considering the positive effects of N-CQDs and OV of $W_{18}O_{49}$, a cooperation of them should be suitable for higher striking photocatalytic performance. Moreover, they have outstanding chemical durability, high dispersity, and excellent compatibility to fabricate hybrid systems.

Based on this, in the present paper N-CQDs were used as seeds to grow $W_{18}O_{49}$ nanocrystals on its surface (N-CQDs@$W_{18}O_{49}$), thus forming a heterojunction photocatalyst with core-shell structure. The "seed-mediated" effect of N-CQDs increased the separation rate of charge carriers in $W_{18}O_{49}$ and promoted the growth of the crystals. Methyl orange (MO) and ciprofloxacin (CIP) were selected as model pollutants to evaluate the photocatalytic activity of the samples under UV–vis and NIR light irradiation.

In a typical experiment, 1 g of citric acid and 3 g of urea were dissolved in 30 mL of water. The above solution was then transferred to a 50 mL Teflon-lined autoclave reactor and heated at 180 °C for 6 h. After filtered and dialyzed for 24 h to remove impurities, and then N-CQDs was freeze-dried to obtain. N-CQDs@$W_{18}O_{49}$ was synthesized through the following steps. First, 0.1 g N-CQDs were dissolved in 100 mL ethanol and stir to obtain a dark yellow solution. Then, 0.8 g WCl_6 was dissolved in 40 mL ethanol to form a light yellow transparent solution. Subsequently, the N-CQDs solution was added into the WCl_6 solution in different volumes, calculate the weight ratio of CQDs to WCl_6, and control the weight ratio at 1%, 3%, 5% and 7%, respectively. Ultimately, the precursor solution was transferred to a 100 mL Teflon-lined high-pressure steam and heated at 240 °C for 20 h. The final products were collected by centrifugation, washed three times with ethanol, and dried in air at 60 °C for 6 h. Composites with variable weight ratios of N-CQDs to $W_{18}O_{49}$ (*i.e.*, 1%, 3%, 5% and 7%) were denoted as N-CQDs@$W_{18}O_{49}$-1, N-CQDs@$W_{18}O_{49}$-3, N-CQDs@$W_{18}O_{49}$-5, and N-CQDs@$W_{18}O_{49}$-7, respectively. Pure $W_{18}O_{49}$ was obtained through the same method, but without N-CQDs. The synthesis process of N-CQDs@$W_{18}O_{49}$ composites is shown in Scheme 1. The sections of N-CQDs@$W_{18}O_{49}$ characterization and photocatalytic activity measurements can be found in Supporting information.

The crystal structures of $W_{18}O_{49}$ and N-CQDs@$W_{18}O_{49}$-5 were analyzed by X-ray diffraction (XRD). As shown in Fig. 1a, the diffraction peaks of 23.48° and 48.02° correspond to (010) and (020) plane of monoclinic $W_{18}O_{49}$. In particular, the (010) diffraction peak from monoclinic $W_{18}O_{49}$ was incredibly strong, which was due to the deviation of $W_{18}O_{49}$ in the [010] direction during the growth process, which was consistent with previous reports [26,27]. In the XRD pattern of N-CQDs@$W_{18}O_{49}$-5 composite, the broadening of (010) plane might be caused by the overlapping of N-CQDs and carbon peak positions. There was a slight change from 47.96° to 45.68° on the plane (020), which might be due to the binding of metal ions in $W_{18}O_{49}$ with N-CQDs. The energy dispersive spectrometer (EDS) elemental mapping results of the CQDs@$W_{18}O_{49}$-5 photocatalyst are shown in Fig. 1b,

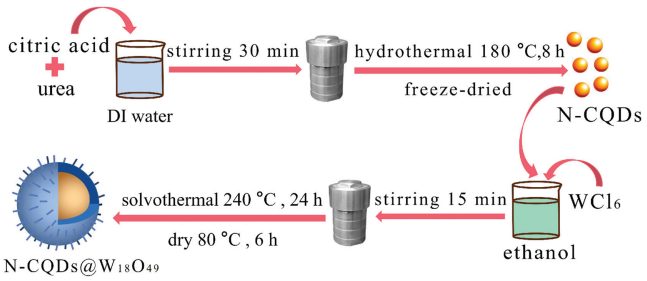

Scheme 1. The prepared route of N-CQDs@$W_{18}O_{49}$ with a facile self-assembly strategy.

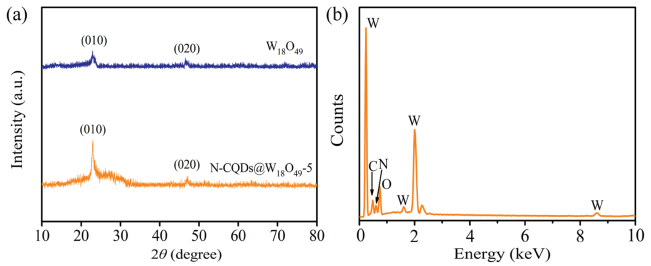

Fig. 1. (a) XRD patterns of $W_{18}O_{49}$ and N-CQDs@$W_{18}O_{49}$-5 samples. (b) EDS analysis of N-CQDs@$W_{18}O_{49}$-5.

revealing that N-CQDs@$W_{18}O_{49}$-5 contained the elements C, N, O and W. The EDS spectrum further confirmed the presence of elements of N-CQDs@$W_{18}O_{49}$ composite.

The morphologies of the prepared samples were characterized by scanning electron microscopy (SEM) and transmission electron microscopy (TEM). As shown in Fig. S1 (Supporting information), the SEM images of $W_{18}O_{49}$ and N-CQDs@$W_{18}O_{49}$ are used to determine the nanostructure, from which we can see that the prepared N-CQDs@$W_{18}O_{49}$ show different shapes as the quality of N-CQDs changed continuously. As for $W_{18}O_{49}$, a rod-like structure can be observed. As shown in Fig. S1, the rod-shaped structure of $W_{18}O_{49}$ became more uniform and thinner with the continuous addition of N-CQDs, which can be attributed to the "seed mediated" effect from N-CQDs. with the solvothermal treatment proceeding, N-CQDs act as nucleation sites, lowering the nuclear energy barrier of $W_{18}O_{49}$ crystal, which accelerates the continuous assembly of $W_{18}O_{49}$ unit cells and presents a typical heterogeneous nucleation process. However, excessive accumulation of N-CQDs leads to aggregation, which further leads to the aggregation of the rod-shaped structure of $W_{18}O_{49}$ (Fig. S1e). In the N-CQDs@$W_{18}O_{49}$-5 composite, $W_{18}O_{49}$ on the surface of N-CQDs shows a more uniform and orderly structure with a thin bar. Fig. S1f is a high-resolution TEM (HRTEM) image of the prepared N-CQDs@$W_{18}O_{49}$-5 composite, and the interplanar spacing of $W_{18}O_{49}$ on N-CQDs is 0.38 nm, which is consistent with the lattice spacing of the monoclinous crystal plane of $W_{18}O_{49}$ (010) [28].

The atomic structure of the prepared $W_{18}O_{49}$ nanomaterials was further studied by Fourier transform infrared (FT-IR) spectroscopy. In Fig. S3a (Supporting information), there are three peaks on the spectrum of N-CQDs, which respectively come from the stretching vibration of C—C (1200 cm^{-1}), the asymmetric and symmetric stretching bands of COO (1540 cm^{-1}), and the stretching mode of —OH (1550 cm^{-1}). The characteristic stretching vibration bands of W=O and O—W—O (500–1000 cm^{-1}) were observed on the spectrum of $W_{18}O_{49}$ (Fig. S3b in Supporting information). After introducing N-CQDs into $W_{18}O_{49}$, the resulting heterostructure of N-CQDs@$W_{18}O_{49}$-5 shows the composite FT-IR signal assigned by $W_{18}O_{49}$ and N-CQDs.

Elemental composition and chemical state of N-CQDs@$W_{18}O_{49}$-5 were investigated by X-ray photoelectron spectroscopy (XPS). The survey XPS spectrum in Fig. S4 (Supporting information) means that the prepared N-CQDs@$W_{18}O_{49}$-5 mainly composed of C, O, and W elements. Fig. S5 (Supporting information) shows the high-resolution spectra of C 1s, N 1s, O 1s and W 4f. As shown in Fig. S5a, the high-resolution spectrum of C 1s can be divided into four peaks located at 284.5, 285.1, 286.3 and 289 eV, respectively. Among them, the peak at 284.5 eV is attributed to C—C/C=C. Peaks of 285.1 eV are C—N/C—O, while peaks of 286.3 eV and 289 eV are C=O and COOH, respectively. Fig. S5b shows the N 1s high-resolution spectrum, which can be divided into three characteristic

peaks located at 398.1, 399.5 and 401.6 eV. Three peaks were attributed to pyridine nitrogen, pyrrole nitrogen, and graphite nitrogen, respectively. The nitrogen elements contained in N-CQDs@$W_{18}O_{49}$-5 samples are mainly nitrogen-containing functional groups on the surface of N-CQDs, which also shows the same conclusion as the N 1s high-resolution spectrum of N-CQDs in Fig. S6. As shown in Fig. S5c, the high-resolution O 1s spectrum of $W_{18}O_{49}$ has two peaks at 529.89 eV and 531.24 eV, corresponding to W—O and OVs. The high-resolution O 1s spectrum of N-CQDs@$W_{18}O_{49}$-5 has three peaks at 529.89, 530.55 and 531.24 eV, corresponding to W—O, C—O/C=O and oxygen vacancy, respectively. C—O/C=O is mainly attributed to the addition of N-CQDs. The peak observed at 529.89 eV corresponds to the lattice oxygen O^{2-} bonded to W [29]. The binding energy of 531.24 eV is attributed to O^{-} or reduced W^{X+}-state connected O^{2-} species [30]. As shown in Fig. S5d, the high-resolution spectrum of W 4f can be divided into three pairs, namely W^{6+}, W^{5+} and W^{4+}. The W $4f_{7/2}$ (35.6 eV) and W $4f_{5/2}$ (37.8 eV) peaks belong to W^{6+}.The peaks of binding energy at 35.21 eV and 37.1 eV are W $4f_{7/2}$ and W $4f_{5/2}$ of W^{5+}, respectively [31]. In addition, the other two small peaks of 34.20 eV (W $4f_{7/2}$) and 36.19 eV (W $4f_{5/2}$) are attributed to w^{4+}. The existence of a low oxidation state (W^{4+}) further confirmed the formation of oxygen vacancies in $W_{18}O_{49}$. As shown in Figs. S5c and d, the peak values of W 4f and O 1s in N-CQDs@$W_{18}O_{49}$-5 move to higher band energies than the corresponding values of $W_{18}O_{49}$. It is worth noting that an increase in binding energy indicates a decrease in electron concentration. Therefore, the change of the characteristic peak binding energy indicates that the electron transfer process will occur on the N-CQDs@$W_{18}O_{49}$-5 heterogeneous interface, and the photogenerated electrons have a tendency to move from $W_{18}O_{49}$ to N-CQDs.

Based on all the experimental results and the above analysis, we propose the growth mechanism shown in Fig. S6 (Supporting information). When the solvent heat treatment started, WCl_6 began to grow on the surface of N-CQDs to form $W_{18}O_{49}$ under high temperature conditions using N-CQDs as seeds. It can be seen from Fig. S7 (Supporting information) that the character of N-CQDs contains a large amount of C—O/C=O, while it can be seen from Fig. S5c that the prepared N-CQDs@$W_{18}O_{49}$-5 appears C—O/C=O. The O atoms of the C—O/C=O unit combine with W^{4+} and W^{5+}, which makes N-CQDs the preferred nucleation site, lowering the nuclear energy barrier of $W_{18}O_{49}$ crystal, and presenting a typical heterogeneous nucleation process, which shows the same result as XRD. It is described as “seed-mediated” effect. With the solvothermal treatment proceeding, the $W_{18}O_{49}$ nucleus on N-CQDs and the low energy there accelerate the continuous assembly of $W_{18}O_{49}$ crystal cells. Herein, N-CQDs induce the heterogeneous nucleation of $W_{18}O_{49}$ lattices and construct a full crystalline hetero-junction photocatalyst.

UV-vis-NIR absorbance spectra were used to characterize the optical response characteristics of different photocatalysts. The quantum effect of N-CQDs and the LSPR effect of $W_{18}O_{49}$, the prepared N-CQDs@$W_{18}O_{49}$ still have obvious light absorption in the UV–vis and NIR regions (Fig. 2a and Fig. S8 in Supporting information). The UV–vis spectrum of N-CQDs shows two absorption bands at 280 and 390 nm (Fig. S8) which correspond to $\pi \rightarrow \pi^*$ transition of the C=C unsaturation and $n \rightarrow \pi^*$ type transition of the C=O respectively. As the De Broglie wavelength, coherence wavelength and baryon Bohr radius of N-CQDs and electrons are comparable, electrons are confined in nano space, electron transport is restricted, electron very short mean free path, and the locality and coherence of electrons are enhanced. These will cause quantum effects. For N-CQDs, when the particle size is equal to or smaller than the Bohr radius of Wannier baryon, they will be in the strong confinement region, which is easy to form baryon and produce baryon absorption band. With the particle size

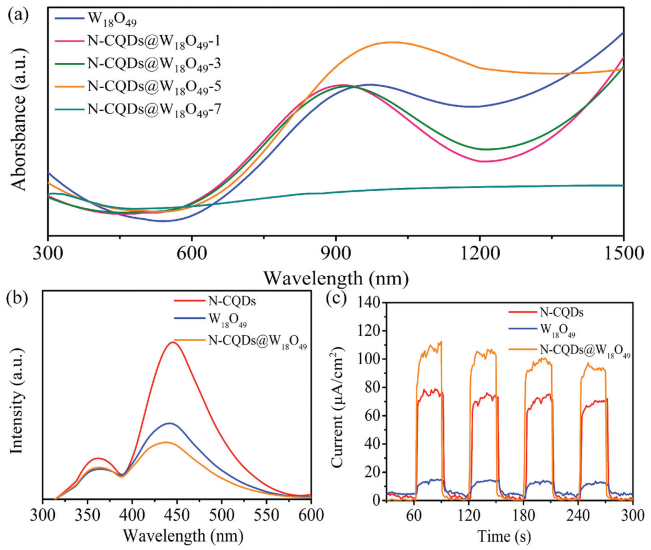

Fig. 2. (a) UV–vis-NIR diffuse reflectance spectra of the prepared $W_{18}O_{49}$ and N-CQDs@$W_{18}O_{49}$ composites. (b) Photoluminescence spectra and (c) photocurrent response.

decreases, quantum effect is triggered, and the lowest energy of the baryon moves toward the high-energy direction, which is a blue shift. In comparison with the pure $W_{18}O_{49}$, the N-CQDs@$W_{18}O_{49}$ shows a blue shift, verifying quantum effect of the N-CQDs sample. Among them, N-CQDs@$W_{18}O_{49}$-5 exhibits strong light absorption under both visible light and NIR light. The UV–vis-NIR absorbance spectra show that N-CQDs@$W_{18}O_{49}$-5 has high sunlight absorption and has potential advantages for enhancing sunlight utilization. Based on the absorption curves, the band gaps of $W_{18}O_{49}$ and N-CQDs@$W_{18}O_{49}$-5 are calculated [32]. According to the results shown in Fig. S9 (Supporting information), the optical band gaps of $W_{18}O_{49}$ and N-CQDs@$W_{18}O_{49}$-5 are 2.81 eV and 2.59 eV, respectively. Compared with $W_{18}O_{49}$, although the bandgap of N-CQDs@$W_{18}O_{49}$-5 is narrowed due to the introduction of N-CQDs, the absorption range of light is enhanced.

PL spectroscopy is an important characterization method for testing charge separation efficiency. Since the luminescence is caused by the rapid recombination between photo-induced e^{-}–h^{+} pairs, high photoluminescence intensity indicates a high recombination rate and low photocatalytic activity. As shown in Fig. 2b, the PL spectra of $W_{18}O_{49}$ and N-CQDs have a strong peak at 440 nm. Due to the addition of N-CQDs, the PL spectrum of N-CQDs@$W_{18}O_{49}$-5 significantly decreases. N-CQDs@$W_{18}O_{49}$-5 has the lowest photocatalytic intensity, indicating the best photocatalytic performance. The photocurrent test results also give a similar conclusion. As shown in Fig. 2c, pure $W_{18}O_{49}$ has the lowest photocurrent response, indicating that $W_{18}O_{49}$ has the lowest defect concentration and the highest charge combination efficiency. It is worth noting that the photocurrent density of N-CQDs@$W_{18}O_{49}$-5 is significantly enhanced compared with the original $W_{18}O_{49}$. Improvements in photocurrent indicate that photo-excited carrier separation in a heterojunction is more effective than using $W_{18}O_{49}$ alone. The above results indicate that N-CQDs injected with $W_{18}O_{49}$ can improve the separation efficiency of photo-induced e^{-}–h^{+} pairs, extend the life of photo-excited carriers and provide a promising photocatalyst for the degradation of pollutants.

In order to investigate the photocatalytic performance of the prepared photocatalytic materials, the dye MO and antibiotic CIP were subjected to photocatalytic degradation under UV–vis and

NIR light. Before the photocatalytic degradation, the adsorption experiment was carried out under dark conditions in order to achieve the adsorption-desorption equilibrium. CIP, as an antibiotic pollutant in the environment, has also been selected as a target pollutant. As shown in Fig. S10a (Supporting information), with the existence of $W_{18}O_{49}$, only 47.3% of CIP can be degraded under UV–vis light irradiation for 180 min. N-CQDs@$W_{18}O_{49}$-5 showed good photocatalytic performance in photodegradation of CIP, and the removal efficiency reached 93.5% after 180 min of UV–vis irradiation. Due to LSPR effect, the photocatalytic activity of $W_{18}O_{49}$ was enhanced under NIR light. We found that the photocatalytic activity of N-CQDs@$W_{18}O_{49}$-5 was still higher than that of the $W_{18}O_{49}$, and the degradation efficiency of N-CQDs@$W_{18}O_{49}$-5 on CIP was 70.6% under NIR irradiation for 180 min. Fig. S10c (Supporting information) shows the result of the degradation of MO by the prepared different photocatalyst under UV–vis irradiation for 120 min. The prepared N-CQDs@$W_{18}O_{49}$-5 has the highest photocatalytic activity, and 97.1% of MO molecules were degraded within 120 min. We found that the photocatalytic activity of N-CQDs@$W_{18}O_{49}$-5 was still higher than that of the $W_{18}O_{49}$, and the degradation efficiency of N-CQDs@$W_{18}O_{49}$-5 on CIP was 72.6% under NIR irradiation for 120 min. At the same time, in the dark reaction process, N-CQDs@$W_{18}O_{49}$-5 also showed a good adsorption effect due to their large specific surface area. It should be noted that excessive or insufficient N-CQDs in the preparation process will cause the ultimate photocatalytic activity to decrease. In addition, the investigation of the photocatalytic degradation kinetics under UV–vis light and NIR light showed that the changes in the concentration of MO and CIP the reaction time in the degradation process of N-CQDs@$W_{18}O_{49}$ are in line with the *pseudo*-first-order kinetics (Fig. S11 in Supporting information). Table S1 (Supporting information) can be seen that the degradation rate of CQDs@$W_{18}O_{49}$-5 is 4 times higher than that of $W_{18}O_{49}$ under UV–vis light. Table S2 (Supporting information) can be seen that the degradation rate of N-CQDs@$W_{18}O_{49}$-5 is 2 times higher than that of $W_{18}O_{49}$ under NIR light. The results show that the N-CQDs@$W_{18}O_{49}$ composite has great potential in the treatment of medical wastewater.

In order to research the mineralization ability of $W_{18}O_{49}$, a total organic carbon (TOC) removal experiment was carried out. As shown in Fig. S12 (Supporting information), under UV–vis light irradiation for 120 min, the TOC removal rate of $W_{18}O_{49}$ is only 23.61%. It is worth noting that under the same conditions, the TOC removal rate of N-CQDs@$W_{18}O_{49}$-5 can reach 45.32%. It can be seen from the above results that the prepared N-CQDs@$W_{18}O_{49}$ material can not only photodegrade CIP molecules but also decompose CIP molecules into CO_2 and H_2O. In practical applications, the reusability and stability of the photocatalyst are very important. Therefore, CIP to evaluate the stability of the prepared N-CQDs@$W_{18}O_{49}$-5 composite in UV–vis and NIR light irradiation. After 5 cycles of experiments, the photocatalytic activity of N-CQDs@$W_{18}O_{49}$-5 did not decrease significantly under UV–vis light and NIR light irradiation (Fig. S13 in Supporting information), indicating that the prepared N-CQDs@$W_{18}O_{49}$ composite has high stability.

According to reports, hydroxyl radicals ($^{\bullet}OH$), superoxide radicals ($O_2^{\bullet-}$) and active hole (h^+) contributed to pollutant oxidation. In order to elucidate the electron transfer and reaction mechanisms in the photocatalytic, radical trapping control experiments were performed on the catalytic degradation of CIP on N-CQDs@$W_{18}O_{49}$ composites. The results of the catalytic performance after radical trapping are presented in Fig. 3a. The addition of 1,4-benzoquinone and EDTA-2Na during the reaction significantly decreased the degradation rate of CIP, indicating that $O_2^{\bullet-}$ and h^+ played an important role in the degradation of CIP under UV–vis light irradiation. In addition, to further explore the

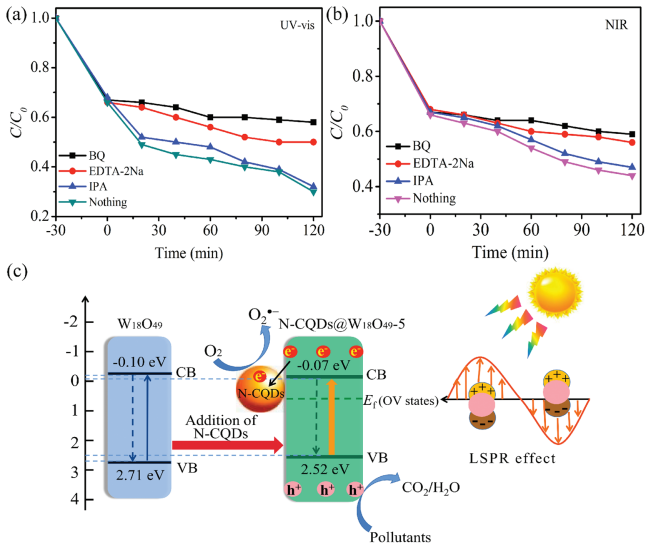

Fig. 3. Trapping experiments for the photocatalytic degradation of CIP under UV–vis (a) and NIR (b) light irradiation. Proposed mechanism for MO and CIP degradation on N-CQDs@$W_{18}O_{49}$-5 under full-spectrum light irradiation (c).

reaction mechanism of the N-CQDs@$W_{18}O_{49}$ composite under NIR light irradiation, capture experiments were carried out under NIR light irradiation ($\lambda > 710$ nm). As shown in Fig. 3b, the photocatalytic degradation of CIP on N-CQDs@$W_{18}O_{49}$-5 was greatly inhibited in the presence of 1,4-benzoquinone and EDTA-2Na, which indicated that $O_2^{\bullet-}$ and h^+ play a major role in the photocatalytic degradation of CIP under NIR light irradiation.

Therefore, based on the above characterization analysis results and photocatalysis experiments, the reaction mechanism of the prepared N-CQDs@$W_{18}O_{49}$-5 composites is proposed and illustrated in Fig. 3c. The bandgap of N-CQDs@$W_{18}O_{49}$-5 is smaller than that of $W_{18}O_{49}$ and it has the highest photocatalytic activity. Therefore, based on the above experimental results, it could be attributed to the photo-generated electrons tend to move to the surface of the N-CQDs, leaving holes in the VB of $W_{18}O_{49}$ under UV–vis. The electrons would be consumed by the adsorbed O_2 and produce $O_2^{\bullet-}$, which acts as the main reactive species to degrade CIP. At the same time, the holes left in the VB of $W_{18}O_{49}$ would directly oxidize CIP as well. Meanwhile, the LSPR effect of $W_{18}O_{49}$ in the NIR region will produce hot electron injection into N-CQDs, increase the electron density on the N-CQDs, and promote the charge separation inside $W_{18}O_{49}$, which promotes the final photocatalytic performance.

In summary, we used a simple solvothermal method and used "seed-mediated" effect to construct a N-CQDs@$W_{18}O_{49}$ core-shell structure, the highly efficient photocatalytic degradation of MO and CIP under UV–vis light and NIR light. N-CQDs are used as seeds to induce precipitation of $W_{18}O_{49}$ crystals. The structure and morphological characteristics indicate that the addition of N-CQDs makes $W_{18}O_{49}$ crystals better form. At the same time, the combination with N-CQDs enhances the separation of photoinduced electron-hole pairs and improves the photocatalytic degradation efficiency of MO and CIP under UV–vis light and NIR light. The radical trap experiments showed that the degradation of CIP was driven mainly by the participation of h^+ and $O_2^{\bullet-}$ radicals. Furthermore, the well crystalline of N-CQDs@$W_{18}O_{49}$ ensure long-term durability and suggest a promising prospect in an application.

Declaration of competing interest

The authors report no declarations of interest.

Acknowledgments

The authors are grateful for financial support from the NSFC project (Nos. 21971057, 61275117), the Outstanding Youth Project of Natural Science Foundation of Heilongjiang Province (No. YQ2019B006) and LBH-Q19052, and the Innovation Foundation of Key Laboratory of Functional Inorganic Material Chemistry, Ministry of Education of China, Natural Science Foundation of Heilongjiang Province of China (No. LH2020E106). The authors thank the members of Key Laboratory of Functional Inorganic Material Chemistry for technical support.

Appendix A. Supplementary data

Supplementary material related to this article can be found, in the online version, at doi:https://doi.org/10.1016/j.cclet.2021.03.018.

References

[1] N. Lu, Z. Zhang, Y. Wang, et al., Appl. Catal. B: Environ. 233 (2018) 19–25.
[2] M. Zhu, L. Zhang, S. Liu, et al., Chin. Chem. Lett. 31 (2020) 1961–1965.
[3] J. Liu, Y. Wei, P. Li, Y. Zhao, R. Zou, J. Phys. Chem. C 121 (2017) 13249–13255.
[4] H. Xu, Y.F. Zhang, X. Lang, Chin. Chem. Lett. 31 (2020) 1520–1524.
[5] Z. Li, Y. Wang, A.A. Elzatahry, et al., Chin. Chem. Lett. 31 (2020) 1598–1602.
[6] D. Wang, H. Zeng, X. Xiong, et al., Sci. Bull. 65 (2020) 113–122.
[7] D.P. DePuccio, P. Botella, B. O'Rourke, C.C. Landry, ACS Appl. Mater. Interfaces 7 (2015) 1987–1996.
[8] J. Wang, L. Tang, G. Zeng, et al., Appl. Catal. B: Environ. 222 (2018) 115–123.
[9] Y. Qin, Y. Guo, Z. Liang, et al., Chin. Chem. Lett. 32 (2021) 1523–1526.
[10] Q. Gao, X. Wu, Y. Kang, J. Alloys Compd. 844 (2020) 155512.
[11] G. Jung, Y. Jeong, Y. Hong, et al., Solid State Electron. 165 (2020) 107747.
[12] C. Feng, L. Tang, Y. Deng, et al., Chem. Eng. J. 389 (2020) 124474.
[13] H. Zuo, J. Tao, H. Shi, et al., Acta Biomater. 80 (2018) 296–307.
[14] Z. Lv, H. Liu, X. Zhang, et al., Physica E 117 (2020) 113719.
[15] C. Feng, L. Tang, Y. Deng, et al., Appl. Catal. B: Environ. 276 (2020) 119167.
[16] Y. Song, J. Bai, R. Zhang, et al., Sens. Actuators B: Chem. 310 (2020) 127671.
[17] A. Farnood, M. Ranjbar, H. Salamati, Int. J. Hydrogen Energy 45 (2020) 1158–1169.
[18] U.A. Rani, L.Y. Ng, C.Y. Ng, E. Mahmoudi, Adv. Colloid Interface Sci. 278 (2020) 102124.
[19] T. Xu, Z. Wan, H. Tang, et al., J. Alloys Compd. 859 (2020) 157784.
[20] X.H. Jiang, L.S. Zhang, H.Y. Liu, et al., Angew. Chem. Int. Ed. 59 (2020) 23112–23116.
[21] M. Gagic, S. Kociova, K. Smerkova, et al., J. Colloid Interface Sci. 580 (2020) 30–48.
[22] B. Han, J. Jiang, Q. Yan, Z. Xin, Q. Yan, Chin. Chem. Lett. 32 (2021) 1–3.
[23] K. Gao, X. Gao, W. Zhu, et al., Chem. Eng. J. 406 (2021) 127155.
[24] H. Yu, J. Huang, L. Jiang, et al., Chem. Eng. J. 402 (2020) 126187.
[25] M. Ji, Y. Liu, J. Di, et al., Appl. Catal. B: Environ. 237 (2018) 1033–1043.
[26] J. Pfeifer, E. Badaljan, P. Tekula-Buxbaum, et al., J. Cryst. Growth 169 (1996) 727–733.
[27] J. Zhang, J. Liu, W. Zhao, et al., J. Alloys Compd. 764 (2018) 1–9.
[28] Z. Zhao, Y. Bai, W. Ning, et al., Appl. Surf. Sci. 471 (2019) 537–544.
[29] Z.X. Cai, H.Y. Li, X.N. Yang, X. Guo, Sens. Actuators B: Chem. 219 (2015) 346–353.
[30] M. Saleem, M.F. Al-Kuhaili, S.M.A. Durrani, et al., Int. J. Hydrogen Energy 40 (2015) 12343–12351.
[31] T. Singh, R. Müller, J. Singh, S. Mathur, Appl. Surf. Sci. 347 (2015) 448–453.
[32] Y. Deng, L. Tang, C. Feng, et al., Appl. Catal. B: Environ. 235 (2018) 225–237.